Volume 17
Number 5
7 February 2025
Pages 2369-2914

# Nanoscale

rsc.li/nanoscale

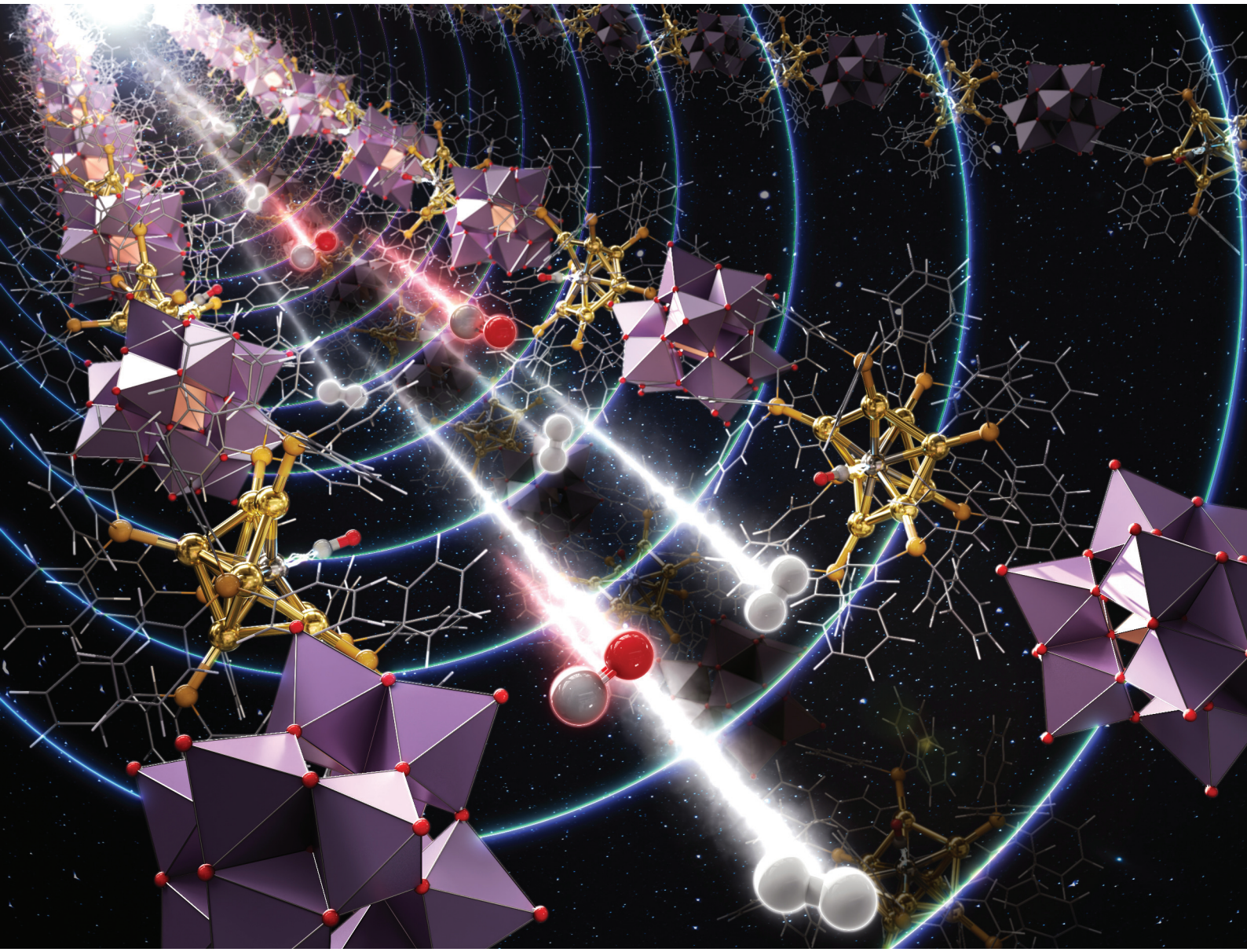

ISSN 2040-3372

ROYAL SOCIETY OF CHEMISTRY

**PAPER**
Seiji Yamazoe *et al.*
*In situ* QXAFS study of CO and $H_2$ adsorption on Pt in $[PtAu_8(PPh_3)_8]$-$H[PMo_{12}O_{40}]$ solid

NCNST

Nanoscale

PAPER

View Article Online
View Journal | View Issue

Check for updates

Cite this: *Nanoscale*, 2025, **17**, 2480

# *In situ* QXAFS study of CO and $H_2$ adsorption on Pt in $[PtAu_8(PPh_3)_8]$-$H[PMo_{12}O_{40}]$ solid†

Tomoki Matsuyama,[a] Taishi Suzuki,[a] Yuto Oba,[a] Soichi Kikkawa,[a] Sayaka Uchida,[b] Junya Ohyama,[c] Kotaro Higashi,[d] Takuma Kaneko,[d] Kazuo Kato,[d] Kiyofumi Nitta,[d] Tomoya Uruga,[d] Keisuke Hatada,[e] Kazuki Yoshikawa,[e] Amelie Heilmaier,[e,f] Kosuke Suzuki,[g] Kentaro Yonesato,[g] Kazuya Yamaguchi,[g] Naoki Nakatani,[a] Hideyuki Kawasoko[a,h] and Seiji Yamazoe*[a]

Received 14th September 2024,
Accepted 14th November 2024

DOI: 10.1039/d4nr03785e

rsc.li/nanoscale

The adsorption behaviors of $H_2$ and CO molecules in crown-motif $[PtAu_8(PPh_3)_8]$-$H[PMo_{12}O_{40}]$ (**PtAu8-PMo12**) solids were investigated by *in situ* quick-scan X-ray absorption fine structure (QXAFS) measurements with a time resolution of 0.1 s. The electronic state of Pt in **PtAu8-PMo12** was drastically changed by the adsorption of $H_2$ and CO molecules because of the formation of Pt–$H_2$/Pt–CO interactions. $H_2$ was adsorbed more rapidly (<0.5 s) on Pt than CO (~2.5 s) and showed reversible adsorption/desorption behavior on Pt atoms in **PtAu8-PMo12**. The rapid adsorption of $H_2$ is due to the fast diffusion of $H_2$, which has a smaller kinetic diameter than CO, in the narrow channels between the closed voids in **PtAu8-PMo12**. Meanwhile, CO was irreversibly adsorbed on Pt, resulting in structural isomerization to the stable "chalice-motif" **PtAu8**, which was determined by XAFS analysis and density functional theory calculations. Structural isomerization was involved by pushing ligands aside to make space for CO adsorption as the void size near Pt in the crown-motif **PtAu8-PMo12** was narrower than the kinetic diameter of CO.

Published on 14 novembre 2024. Downloaded on 20/12/2025 2:52:36.

## Introduction

Metal clusters composed of <100 atoms have attracted significant attention because of their quantized electronic states and unique geometric structures that cannot be predicted from their bulk materials.[1–4] The electronic state of metal clusters, which determines their functions, depends on the number of metal atoms and their geometric structures. Therefore, atomically precise synthesis of metal clusters is essential to understand the relationship between functions and structures.[5,6] To date, numerous ligand-protected metal clusters composed of Au, Ag, and Cu, among others, have been synthesized in a liquid phase. For example, Au ions are reduced in the presence of different protecting ligands, like phosphine,[7] thiolate,[8] alkynyl,[9] and N-heterocyclic carbene,[10] which allows the synthesis of ligand-protected Au clusters with a highly homogeneous size distribution. Ligand-protected Au clusters have unique electronic structures depending on their size and composition, and exhibit optical properties,[11,12] photoluminescence,[13] magnetism,[14] and redox activity.[15]

The ligand-protected metal clusters have been applied as catalysts, such as for the selective oxidation of styrene by phosphine-protected $Au_{11}(PR_3)_7Cl_3$ and $[Au_{11}(PR_3)_8Cl_2]^+$ (R = alkyl groups)[16] or by thiolate-protected $Au_{25}(SR)_{18}$, $Au_{38}(SR)_{24}$ and $Au_{144}(SR)_{60}$[17] as well as methane oxidation by mixed ligand-protected $[Au_{24}(PR_3)_{10}(SR)_5Cl_2]^-$ and $[Au_{25}(PR_3)_{10}(SR)_5Cl_2]^{2-}$.[18] Heterometal doping is one of the most effective methods for controlling and inducing the reactivities of ligand-protected Au clusters because metal dopants can modulate the electronic state of the clusters. The hydrogen evolution reaction has been accelerated by Pt single-atom doping to $[Au_{25}(SR)_{18}]^-$ because

[a]Department of Chemistry, Graduate School of Science, Tokyo Metropolitan University, 1-1 Minami-osawa, Hachioji-shi, Tokyo 192-0397, Japan. E-mail: yamazoe@tmu.ac.jp
[b]Department of Basic Science, School of Arts and Sciences, The University of Tokyo, 3-8-1 Komaba, Meguro-ku, Tokyo 153-8902, Japan
[c]Faculty of Advanced Science and Technology, Kumamoto University, 2-39-1 Kurokami, Chuo-ku, Kumamoto-shi, Kumamoto 860-8555, Japan
[d]Center for Synchrotron Radiation Research, Japan Synchrotron Radiation Research Institute (JASRI), 1-1-1, Kouto, Sayo-cho, Sayo-gun, Hyogo 679-5198, Japan
[e]Department of Physics, University of Toyama, 3190 Gofuku, Toyama 930-8555, Japan
[f]Department of Chemistry, Ludwig-Maximilians-Universität (LMU), Butenandtstr. 5-13, 81377 Munich, Germany
[g]Department of Applied Chemistry, School of Engineering, The University of Tokyo, 7-3-1 Hongo, Bunkyo-ku, Tokyo 113-8656, Japan
[h]Precursory Research for Embryonic Science and Technology (PRESTO), Japan Science and Technology Agency (JST), 7, Gobancho, Chiyoda-ku, Tokyo 102-0076, Japan

† Electronic supplementary information (ESI) available: Fig. S1–S15, Scheme S1 and Tables S1–S3. See DOI: https://doi.org/10.1039/d4nr03785e


This journal is © The Royal Society of Chemistry 2025

Published on 14 novembre 2024. Downloaded on 20/12/2025 2:52:36.

of the depletion of two valence electrons and a positive shift in reduction potential.[19] Phosphine-protected $MAu_{12}(PRP)_5Cl_2$ (M = Au, Pd, Pt, Ru, Rh, Ir) also showed a change in electronic structure depending on the central dopant.[20] In particular, photoinduced intermolecular [2 + 2] cycloaddition of bisenone was shown to be promoted by Pt- and Ir-doped $MAu_{12}(PRP)_5Cl_2$.[21] Metal dopants often provide new active sites.

Among the ligand-protected metal clusters, phosphine-protected $[Au_9(PR_3)_8]^{3+}$ (**Au9**) with a crown-motif structure has a coordinatively unsaturated Au atom located at the center of **Au9**.[22] Although the molecule can access the central Au in **Au9**, no reports have described that the molecule is activated by **Au9**. Meanwhile, $[PtAu_8(PR_3)_8]^{2+}$ (**PtAu8**) with a crown-motif structure, in which the central Au in **Au9** is substituted by Pt, worked as a catalyst for the $H_2$–$D_2$ exchange reaction.[23] In addition, **PtAu8** in the solution state exhibited the nucleophilic adsorption of small molecules, such as CO.[24] These reactivities have also been reported for Pt-centered Au clusters, such as $[PtAu_9(PR_3)_9]^{3+}$ and $[(PR_3)PtAu_6(PR_3)_6]^{2+}$.[25,26] However, the molecular adsorption on solid ligand-protected metal clusters has been limited.

Our group focused on **Au9** and heterometal-doped $[MAu_8(PPh_3)_8]^{2+}$ (**MAu8**, M = Pt, Pd) to investigate thermal stabilities[27] and control their geometric structures using counter anions.[28] Recently, crown-motif **Au9** and **MAu8** were synthesized by associating anionic $[PMo_{12}O_{40}]^{3-}$ (**PMo12**) polyoxometalate with cesium chloride crystal packing structures.[27] The **Au9-PMo12** and $[MAu_8(PPh_3)_8]$-$H[PMo_{12}O_{40}]$ (**MAu8-PMo12**) were thermally stable at <473 K.[27] The crystal structure of **PtAu8-PMo12** is shown in Fig. 1. Two types of voids of different sizes can be observed in the crystals. The large void ($V_L$) is in the *ab*-plane, and **PtAu8** is surrounded by $4V_L$. The small void ($V_S$) is located over the Pt atom in **PtAu8**. $H_2$ and CO are linear diatomic molecules of different sizes and thus can be used as probe molecules to reveal the reactivity of solid ligand-protected metal clusters in porous crystals with small voids. Interestingly, we found that small molecules, such as $H_2$ and CO, could diffuse into the **PtAu8-PMo12** solid although these voids are isolated and there is no path for the molecules to diffuse into the crystal.

This study focuses on the $H_2$ and CO adsorption/desorption properties of **PtAu8-PMo12** solids. The interaction of the central Pt for **PtAu8** with $H_2$/CO was monitored by *in situ* quick-scan X-ray absorption fine structure (QXAFS) analysis because the peak intensity and energy assigned to 2p–5d electron transition were changed by the interaction of Pt with the molecule.[30] We found that both $H_2$ and CO could diffuse into **PtAu8-PMo12** solid and interact with Pt of **PtAu8** core, whereas **Au9-PMo12**, which had the same crystal structure as **PtAu8-PMo12**, could not interact with $H_2$ and CO. The adsorption rate of $H_2$ on Pt is more than four times higher than that of CO in **PtAu8-PMo12**, suggesting that the diffusion of molecules in **PtAu8-PMo12** solids is a key process for molecular adsorptions and small $H_2$ can pass through the narrow channels more easily than CO.

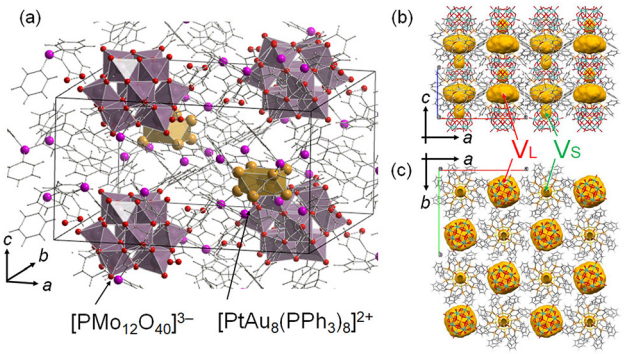


**Fig. 1** (a) Crystal structure of **PtAu8-PMo12**.[27] Void analysis of **PtAu8-PMo12** in the (b) *ac*-plane and (c) *ab*-plane. Void space (in yellow) is depicted with a probe radius of 1.2 Å using the CSD Mercury software.[29]

## Results and discussion

The synthesis of $[PtAu_8(PR_3)_8](NO_3)_2$ (**PtAu8-NO3**) was confirmed by ESI-MS and UV-Vis spectroscopy. As shown in Fig. 2a, a strong divalent molecular ion peak was observed at $m/z$ = 1935.1. This isotopic pattern was consistent with the pattern calculated as $[PtAu_8(PPh_3)_8]^{2+}$. Fig. 2b shows the UV-Vis spectrum of the **PtAu8-NO3** methanol solution. The broad band at 500–570 nm and the peaks at 428, 354, and 306 nm were in accordance with the absorption properties of the **PtAu8-NO3** solution with the crown-motif structure.[31] **PtAu8-PMo12** synthesized by anion exchange was characterized by DR-UV-Vis spectroscopy and powder XRD. A broad band at

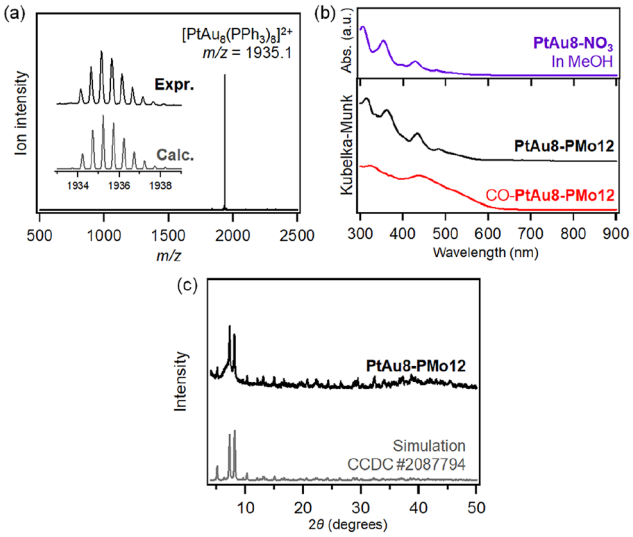


**Fig. 2** Characterizations of **PtAu8-NO3** and **PtAu8-PMo12**. (a) Positive-ion mode ESI-MS of the acetonitrile solution of **PtAu8-NO3**. (b) UV-Vis spectrum of methanolic solution of **PtAu8-NO3** and DR-UV-Vis spectra of **PtAu8-PMo12** and CO adsorbed **PtAu8-PMo12**. (c) Powder-XRD patterns of **PtAu8-PMo12** and simulated **PtAu8-PMo12** (CCDC 2087794).

Published on 14 nuvembre 2024. Downloaded on 20/12/2025 2:52:36.

500–570 nm and peaks at 434, 361, and 313 nm observed in the **PtAu8-PMo12** solid were consistent with those of the crown-motif structure.[28] The powder XRD pattern of the **PtAu8-PMo12** solid had diffraction peaks at $2\theta$ = 5.12, 7.25, and 8.09 degrees, as shown in Fig. 2c. These results indicate that the **PtAu8-PMo12** solid had a CsCl-type crystal structure.[28] In addition, local structures of **PtAu8-PMo12** were determined by curve fitting analysis of Au $L_3$- and Pt $L_3$-edges EXAFS spectra at 10 K (Fig. S1 and S2†). The average coordination numbers (CNs) for Au–P (CN = 1.4 ± 0.2), Au–Pt (CN = 1.4 ± 0.1), and Au–Au bonds (CN = 2.3 ± 0.2) obtained by Au $L_3$-edge FT-EXAFS analysis, and for Pt–Au (CN = 7.8 ± 0.3) obtained by Pt $L_3$-edge FT-EXAFS analysis revealed that the **PtAu8** in **PtAu8-PMo12** had a crown-motif structure with the central atom of Pt (Tables S1 and S2†). Similar characterizations were conducted for **Au9-PMo12** (Fig. S1, S3 and Table S1†). From the above results, we concluded that **PtAu8-PMo12** and **Au9-PMo12** solids with crown-motif structures were synthesized.

We investigated the molecular adsorption properties of crown-motif **PtAu8-PMo12** using Pt $L_3$-edge XAFS measurements. The Pt $L_3$-edge XANES of **PtAu8-PMo12** is shown in Fig. 3a. The peak appearing in the absorption edge at 11 569.6 eV was assigned to the electron transition from Pt 2p to unoccupied 5d orbitals.[32] The peak energy and intensity were changed by the introduction of CO, as shown in Fig. 3a. The time course of the peak intensity at 11 570 eV is shown in Fig. 3b. The peak intensity was increased by CO introduction within 2.5 s. The peak energy at the absorption edge shifted from 11 569.6 eV to 11 570.5 eV. These changes are due to the formation of Pt 5d–C 2p antibonding hybrid orbitals and electron donation from Pt to CO upon CO adsorption on the central Pt of the **PtAu8** cluster (discussed later). No shape changes in the Pt $L_3$-edge XANES were observed upon exposure to a vacuum after CO introduction, as shown in Fig. 3a. Meanwhile, the crown-motif **Au9-PMo12**, which also had a CsCl-type crystal structure (as shown in Fig. S4a†) with an Au center in the crown-motif **Au9**, did not adsorb CO under the same conditions because no change in Au $L_3$-edge XANES and EXAFS was detected before and after CO introduction, as shown in Fig. S4b–d.† We also performed Pt $L_3$-edge *in situ* XANES measurements for **PtAu8-NO3** acetonitrile solution, of which Pt atoms reacted with $H_2$ and CO (Fig. S5†). The XANES spectra of the solution sample showed similar changes in the white line intensity compared with that of solid **PtAu8-PMo12**; thus, we consider that CO and $H_2$ adsorption on Pt occurs on the crystal surface and inside the crystal. These results suggest that the CO diffuses into solid **PtAu8-PMo12** and strongly interacts with Pt of the crown-motif **PtAu8**.

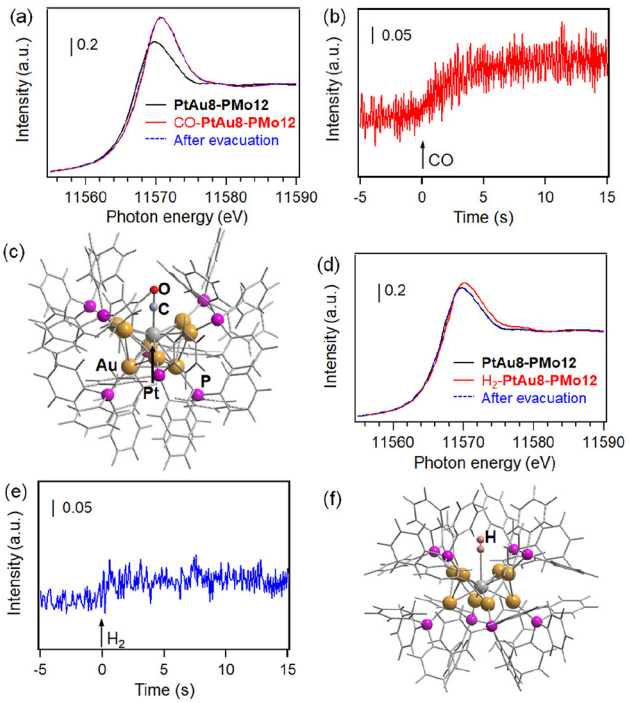


**Fig. 3** (a) Pt $L_3$-edge XANES spectra of **PtAu8-PMo12**, CO-introduced **PtAu8-PMo12**, and after evacuation. (b) Time course of peak intensity at 11 570 eV in Pt $L_3$-edge XANES of **PtAu8-PMo12** during CO introduction. (c) Optimized structure of CO-**PtAu8** by DFT calculation. (d) Pt $L_3$-edge XANES spectra of **PtAu8-PMo12**, $H_2$-introduced **PtAu8-PMo12**, and after evacuation. (e) Time course of peak intensity at 11 570 eV in Pt $L_3$-edge XANES of **PtAu8-PMo12** during $H_2$ introduction. (f) Optimized structure of $H_2$-**PtAu8** by DFT calculation.

Because it is known that CO adsorbed on **PtAu8** in solution to form $[Pt(CO)Au_8(PPh_3)_8]^{2+}$,[24] the structure of **PtAu8-PMo12** after CO introduction (CO-**PtAu8-PMo12**) was investigated by ESI-MS, UV-Vis, XAFS, and DFT calculations. The ESI-MS spectrum of CO-**PtAu8-PMo12** is shown in Fig. S6.† The $[(CO)PtAu_8(PPh_3)_8]^{2+}$ was detected, suggesting that CO adsorbed on **PtAu8** in a solid form. The DR-UV-Vis spectra of **PtAu8-PMo12** before and after CO introduction indicated that the optical properties were changed by CO introduction (Fig. 2b), and a peak at 430 nm and shoulder peak at 520 nm appeared. The optical properties of CO-**PtAu8-PMo12** resembled those of $[Pt(CO)Au_8(PPh_3)_8]^{2+}$ in an ethanol solution, as shown in Fig. S7.† The stable structure of CO-adsorbed **PtAu8** (CO-**PtAu8**) calculated by DFT is shown in Fig. 3c. The stable structure, with a "chalice-motif" structure, was in accordance with $[Pt(CO)Au_8(PPh_3)_8]^{2+}$ in solution, as reported previously.[24] The absorption peaks of CO-**PtAu8-PMo12** at 430 and 530 nm were reproduced by TDDFT calculations using the calculated CO-**PtAu8** structure, as shown in Fig. S7.† Au $L_3$- and Pt $L_3$-edge EXAFS and FT-EXAFS revealed that the crown-motif structure of **PtAu8-PMo12** was changed by CO introduction, as shown in Fig. S8.† Curve fitting analysis revealed that CNs and the bonding distances of Au–P (1.0 ± 0.2, 2.23 ± 0.03 Å), Au–Pt (1.3 ± 0.1, 2.69 ± 0.02 Å), and Au–Au (3.6 ± 0.7, 2.93 ± 0.11 Å) in Au $L_3$-edge and CNs and the bonding distances of Pt–C (1.3 ± 0.3, 1.81 ± 0.10 Å), Pt–Au (8.0 ± 0.4, 2.64 ± 0.03 Å) in Pt $L_3$-edge of CO-**PtAu8-PMo12** agreed with those obtained from the calculated CO-**PtAu8**, as shown in Tables S1, S2 and S3.† In addition, the absorption edge peak appearing in the Pt $L_3$-edge XANES shifted to a high-energy region by CO adsorption (Fig. 3a). The simulated Pt $L_3$-edge XANES of the crown-motif **PtAu8** and the chalice-motif CO-**PtAu8** (using the structure in

 This journal is © The Royal Society of Chemistry 2025

Published on 14 nuvembre 2024. Downloaded on 20/12/2025 2:52:36.

Fig. 3c) revealed that the peaks in the absorption edge of CO-**PtAu8** appeared at a higher-energy region than those of the crown-motif **PtAu8** (Fig. S9†). These results indicate that CO diffused into the **PtAu8-PMo12** solid and that one CO was adsorbed on the central Pt of **PtAu8**.

$H_2$ adsorption behavior was also investigated by Pt $L_3$-edge XANES of **PtAu8-PMo12** solids. The Pt $L_3$-edge XANES spectra of **PtAu8-PMo12** before and after $H_2$ introduction are shown in Fig. 3d. The peak at 11 569.6 eV was slightly shifted to 11 570.2 eV and increased by $H_2$ introduction because of the formation of the hybrid orbital of Pt 5d–H 1s.[30] The time course of peak intensity at 11 570 eV is shown in Fig. 3e. Interestingly, the peak intensity was immediately changed within 500 ms by $H_2$ introduction, which was faster than that of CO adsorption. The Pt $L_3$-edge XANES of **PtAu8-PMo12** returned to its original state after $H_2$ evacuation, as shown in Fig. 3d. After $H_2$ evacuation, $H_2$ was reintroduced into **PtAu8-PMo12**. The $H_2$ again interacted with Pt within 500 ms, and the Pt $L_3$-edge XANES of the second $H_2$-adsorbed **PtAu8-PMo12** was in good agreement with that of the first one. The changes in Pt $L_3$-edge XANES shape corresponding to the $H_2$ adsorption and desorption were repeated four times, as shown in Fig. S10.† Meanwhile, the crown-motif **Au9-PMo12**, as shown in Fig. S4,† did not interact with $H_2$ under the same conditions because no change in Au $L_3$-edge XANES was detected before and after $H_2$ introduction, as shown in Fig. S11.† Therefore, we found that $H_2$ adsorption/desorption proceeded reversibly on Pt in **PtAu8-PMo12**.

The structure of $H_2$-adsorbed **PtAu8** in **PtAu8-PMo12** was investigated by Au $L_3$-edge EXAFS, as shown in Fig. S12.† Changes in the EXAFS oscillations of **PtAu8-PMo12** before and after $H_2$ adsorption were not observed. The DFT calculation of $H_2$ adsorption on Pt at end-on while maintaining the crown-motif **PtAu8** in Fig. 3f also demonstrated that there was no conformational change due to $H_2$ adsorption.

Next, the diffusion of CO and $H_2$ molecules into **PtAu8-PMo12** solids is discussed. **PtAu8-PMo12** possesses two types of closed voids, $V_L$ (8.9 Å × 8.9 Å × 5.3 Å) and $V_S$ (3.1 Å × 3.1 Å × 4.0 Å), as shown in Fig. 1 and S13.† The large void, $V_L$, is in the *ab*-plane, and **PtAu8** is surrounded by four $V_L$. The small void, $V_S$, is located over the Pt atom in **PtAu8**. Considering that the kinetic diameters of $H_2$ and CO, which are empirically used for gas adsorption, are 2.89 Å and 3.76 Å, respectively,[33] $V_L$ has a sufficient size for both $H_2$ and CO, whereas $V_S$ can only accept $H_2$. Interestingly, the neighbouring $V_L$–$V_L$ in the *ab*-plane and $V_L$–$V_S$ in the *ac*- or *bc*-plane are connected by a narrow channel (diameter of 1.6–2.2 Å), as shown in Fig. 4. Uchida's group reported that an ionic crystal composed of polyoxometalate and metal complex could absorb $Cs^+$ (ion radius: 3.1 Å) by the diffusion between the closed voids due to the flexibility of the crystal lattice.[34] Identically, $H_2$ and CO can reach Pt of **PtAu8** by diffusing between the closed voids through the narrow channels, as shown in Fig. 4, owing to the flexibility of the ligands of **PtAu8**. After the molecules diffuse into the $V_L$ in the *ab*-plane through narrow **path 1** in Fig. 4, some of the molecules move to $V_S$ through **path 2** in Fig. 4. In

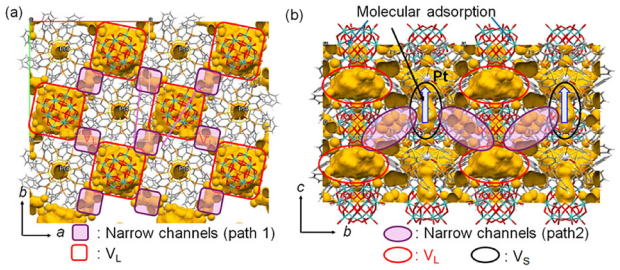


**Fig. 4** Void spaces and narrow channels in **PtAu8-PMo12**: views of (a) *ab*- and (b) *bc*-planes. A probe radius of 0.8 Å was used to visualize the narrow channels.

the case of $H_2$ adsorption/desorption, the $V_S$ over **PtAu8**, which is the void through which Pt is accessed, is larger than $H_2$. Therefore, $H_2$ adsorbs/desorbs on/from Pt without structural changes. Pignolet's group reported that the $H_2$–$D_2$ exchange reaction proceeded on the Pt of **PtAu8**.[23] However, they did not determine the adsorption site of $H_2$ experimentally or mention the $H_2$ diffusion into a solid. We demonstrated that $H_2$ diffused into the **PtAu8-PMo12** solid and was adsorbed on Pt in **PtAu8** without structural change.

We also demonstrated that CO, which is larger than $H_2$, diffused into the **PtAu8-PMo12** solid and adsorbed on Pt, despite the $V_S$ being smaller than a CO molecule. Because the adsorbed CO did not desorb under vacuum conditions (Fig. 3a), CO was strongly adsorbed on Pt. Therefore, it is expected that the crown-motif structure isomerized to the chalice-motif structure to make space to adsorb CO on Pt, as shown in Fig. 3c. Steggerda's group reported that CO reacted with **PtAu8** in solution to obtain the chalice-motif $[Pt(CO)Au_8(PPh_3)_8]^{2+}$.[24] In addition, the structural isomerization from crown-motif to chalice-motif is achieved by small changes in cluster size and $(3AuPPh_3)$–Pt–$(3AuPPh_3)$ angle, as shown in Scheme S1.† Therefore, the chalice-motif $[Pt(CO)Au_8(PPh_3)_8]^{2+}$ can be formed by CO adsorption on crown-motif **PtAu8-PMo12** with structural isomerization even in the solid phase.

The *in situ* QXAFS measurements revealed that $H_2$ adsorption on Pt of **PtAu8-PMo12** occurred faster than CO adsorption, as shown in Fig. 3b and e. The adsorption rate depends on the adsorption energy and/or diffusion path. The adsorption/desorption studies clearly showed that the interaction between $H_2$ and Pt was weaker than that between CO and Pt because $H_2$ was reversibly adsorbed/desorbed, whereas CO was not desorbed under the same conditions. The $H_2$ adsorption energy (difference in the Gibbs free energies) on Pt of the crown-motif **PtAu8** was calculated to be a positive value (0.33 eV) due to the effect of entropy because the difference in the adsorption enthalpies was −0.035 eV, which was similar to $H_2$ adsorption energies on metal clusters.[35] The Pt–H bond length of 2.902 Å in $H_2$-**PtAu8** is longer than the Pt–H bond (1.646 Å) in hydride-adsorbed H-**PtAu8**[36] calculated by DFT, as shown in Fig. S14.† Therefore, the interaction between $H_2$ and **PtAu8** is weak, and adsorbed $H_2$ is desorbed under vacuum conditions.

Published on 14 nuvembre 2024. Downloaded on 20/12/2025 2:52:36.

The reason that the CO did not desorb from **PtAu8-PMo12** under vacuum conditions is that the CO adsorption energy was calculated to be −0.73 eV, which means that CO-**PtAu8** is more stable than crown-motif **PtAu8** with CO and is the driving force for structural isomerization. The calculated Pt-CO length of 1.91 Å in CO-**PtAu8** is in the range of typical coordination bonds. Therefore, CO adsorption occurs as chemisorption, while $H_2$ adsorption occurs as physisorption. These results clearly explained the trends between $H_2$ and CO adsorption/desorption although the $H_2$ adsorption rate was not explained by the adsorption energy.

The molecular diffusion in a solid depends on the diffusion path, void size, and molecular size. From the above discussion, there is no difference in the diffusion path through which the two molecules diffuse. However, molecules must pass through the narrow channels (**paths 1** and **2**) with a diameter of 1.6–2.2 Å to reach the Pt sites in **PtAu8-PMo12**. Because the kinetic diameter of $H_2$ (2.89 Å) is smaller than that of CO (3.76 Å), $H_2$ diffuses in the narrow channel more easily than CO. In addition, CO needs to push the ligands aside to make space for adsorption on Pt because the $V_S$ is narrower than the kinetic diameter of CO. We concluded that the molecular adsorption rate in **PtAu8-PMo12** depends on the diffusion between closed voids and that the smaller molecule, $H_2$, shows more rapid adsorption on Pt in **PtAu8-PMo12** than CO, which must make space for adsorption by pushing ligands aside.

This work indicates that the gas diffusion rates of $H_2$ and CO of **PtAu8-PMo12** differ due to the size of the molecules and voids. In addition, we demonstrated that the optical properties of the clusters could be changed by CO adsorption with structural isomerization. The void size was controlled by the combination of cationic ligand-protected metal clusters and anionic metal oxide clusters with different sizes and compositions. Thus, the void-engineering of composite clusters and/or control of optical properties by molecular adsorption leads to the development of gas separation and/or gas sensors.

## Conclusions

In this study, we investigated the molecular adsorption behaviors of crown-motif **PtAu8-PMo12** solid by *in situ* QXAFS measurements with a time resolution of 0.1 s. Pt $L_3$-edge XANES spectra showed that CO was irreversibly adsorbed on the Pt site with structural isomerization to the chalice-motif structure in solid form. Meanwhile, $H_2$ was reversibly adsorbed/desorbed on Pt without a structural change. The adsorption rate of $H_2$ (<0.5 s) on Pt in **PtAu8-PMo12** was faster than that of CO (~2.5 s), whereas the interaction of Pt–$H_2$ was weaker than that of Pt–CO. The void analysis revealed that **PtAu8-PMo12** with CsCl-type crystal packing has two types of closed voids with a large void, $V_L$, being in the *ab*-plane and **PtAu8** being surrounded by four $V_L$, and a small void, $V_S$, being located over the Pt atom in **PtAu8**. $H_2$/CO could diffuse between the closed voids through the narrow channels (1.6–2.2 Å) of **PtAu8-PMo12** and is adsorbed on Pt from the $V_S$ space. Because the kinetic diameter of $H_2$ (2.89 Å) is smaller than that of CO (3.76 Å), $H_2$ diffuses in the narrow channel more easily than CO. In addition, CO needs to push the ligands aside to create space for adsorption on Pt. From these results, we concluded that the molecular adsorption rate is governed by the diffusion process of molecules in **PtAu8-PMo12**. Therefore, the smaller molecule, $H_2$, shows more rapid adsorption on Pt in **PtAu8-PMo12** compared with CO.

## Experimental

### Chemicals

All reagents used in this study were commercially available. Hydrogen tetrachloroaurate(III) tetrahydrate ($HAuCl_4{\cdot}4H_2O$, 99.0%) was purchased from Kanto Chemical Co., Inc. Tetrabutyl ammonium bromide {TBABr: $[N(C_4H_9)_4]Br$, >98.0%}, triethylamine [TEA: $N(C_2H_5)_3$, >99.0%], and tetrakis (triphenylphosphine)platinum(0) [$Pt(PPh_3)_4$, >97.0%] were purchased from Tokyo Chemical Industry Co., Ltd. Sodium borohydride ($NaBH_4$, 95.0%), triphenylphosphine ($PPh_3$, 97.0%), phosphomolybdic acid hydrate {$H_3[PMo_{12}O_{40}]{\cdot}nH_2O$, >95.0%}, and acetic anhydride [$(CH_3CO)_2O$, >97.0%] were purchased from Wako Pure Chemical Industry.

### Synthesis of $[Au_9(PPh_3)_8](NO_3)_3$ (Au9-NO3)

Undoped **Au9-NO3** was prepared in accordance with the literature.[37] First, 0.6 mmol of $Au(PPh_3)NO_3$, synthesized by anion exchange from $Au(PPh_3)Cl$, was dispersed in 24 mL of ethanol. 0.2 mmol of $NaBH_4$ dissolved in 14 mL of ethanol solution was added to this suspension dropwise. After stirring at room temperature for 2 h, the brown solution was filtered through a membrane filter (pore size = 0.20 μm). The filtrate was evaporated to dryness and redissolved in dichloromethane (5 mL). The solution was filtered and dried, and the precipitate was washed with tetrahydrofuran and hexane. Finally, it was vacuum dried to produce a green powder.

### Synthesis of $[PtAu_8(PPh_3)_8](NO_3)_2$ (PtAu8-NO3)

**PtAu8-NO3** was synthesized in accordance with the literature.[31] Here, 0.2 mmol of $Pt(PPh_3)_3$ obtained by heat treatment of $Pt(PPh_3)_4$ [27] was placed in a glass container with 1.0 mmol of $Au(PPh_3)NO_3$. Next, 20 mL of THF was added, and a small amount of $H_2$ gas was bubbled while stirring at room temperature. Note that an excessive flow rate results in the formation of $[PtAu_6(PPh_3)_7](NO_3)_2$ as a byproduct. The red-orange precipitate was gathered by centrifugation (2500 rpm) and washed with a mixture of a small amount of dichloromethane and a large amount of diethyl ether three times. After vacuum drying, 169 mg of red-orange powder was dissolved in 10 mL of dichloromethane with 52 mg of $Au(PPh_3)NO_3$. Then, 0.2 mmol of TEA was added to the solution with stirring. After 24 h, this solution was evaporated and washed with diethyl ether. Finally, a brown solid was obtained after vacuum drying.

 This journal is © The Royal Society of Chemistry 2025

Published on 14 nuvembre 2024. Downloaded on 20/12/2025 2:52:36.

### Synthesis of $TBA_3[PMo_{12}O_{40}]$ (TBA-PMo12)

**TBA-PMo12** was synthesized by cation exchange reaction.[37] Here, 0.3 mmol of $H_3[PMo_{12}O_{40}]\cdot nH_2O$ was dissolved in 50 mL of pure water. Next, 1.2 mmol of solid form TBABr was added to this solution. After stirring for 0.5 h at room temperature, the yellow precipitate was collected by centrifugation (3500 rpm) and washed with pure water. The precipitate was then reprecipitated using 5 mL of acetone and 45 mL of hexane. Finally, it was vacuum dried to produce yellow powder.

### Synthesis of Au9-PMo12 and PtAu8-PMo12

**Au9-PMo12** and **PtAu8-PMo12** were synthesized in the same way as previously reported.[28] Here, 0.016 mmol of **TBA-PMo12** dissolved in 20 mL of acetonitrile was added at room temperature to 0.010 mmol of **Au9-NO3**/**PtAu8-NO3** solution (40 mL of acetonitrile). After 30 min of stirring, the precipitate was collected by centrifugation (2500 rpm) and washed with acetonitrile three times. Finally, it was vacuum-dried to give **Au9-PMo12** and **PtAu8-PMo12** solids.

### Characterizations

The synthesized ligand-protected metal clusters, polyoxometalates, and their composites were analyzed by ultraviolet-visible (UV-Vis) spectroscopy, electrospray ionization (ESI) mass spectrometry, and powder X-ray diffraction (XRD). The UV-Vis spectra of **PtAu8-NO3** and **Au9-NO3** in methanol and ethanol solutions of CO-adsorbed **PtAu8**, which were synthesized by reacting CO with **PtAu8-NO3** in ethanol, were measured in transmittance mode (V-770; Jasco). The UV-Vis spectra of the solid states of **PtAu8-PMo12**, **Au9-PMo12**, and CO-adsorbed **PtAu8-PMo12** were recorded using an integrating sphere unit in diffuse reflectance (DR) mode. The ESI mass spectra of **PtAu8-NO3** and **Au9-NO3** in acetonitrile were measured in positive-ion mode using a time-of-flight mass spectrometer (microTOF-II; Bruker). The powder XRD patterns of the composite metal clusters were determined using a powder X-ray diffractometer with Cu Kα radiation (MiniFlex600; Rigaku).

The XAFS spectra of **PtAu8-PMo12** and **Au9-PMo12** were measured at the BL01B1 beamline of the SPring-8 facility operated by the Japan Synchrotron Radiation Research Institute. Si (111) double-crystal monochromators were employed to obtain the incident X-ray beam for Pt $L_3$- and Au $L_3$-edge XAFS measurements. All solid cluster samples were mixed with boron nitride as a diluent using an agate mortar. These mixtures were pressed into pellets. For Pt $L_3$- and Au $L_3$-edge XAFS measurements at 10 K, the pellets were mounted in a copper holder attached to a cryostat. To investigate the molecular adsorption behavior, quick-scan XAFS measurements (QXAFS) under transmission mode were performed at the BL36XU beamline of SPring-8 with a time resolution of 100 ms.[38] A Si (220) channel-cut crystal monochromator was used to obtain the incident X-rays. Pt $L_3$- and Au $L_3$-edge *in situ* XAFS measurements were carried out using the pelletized samples mounted on an *in situ* cell connected to a gas-introducing apparatus (Fig. S15†). Approximately 15 mg solid cluster samples were mixed with 50 mg of boron nitride and pressed into $\varphi$7 pellet. To maintain gas diffusion in the solid cluster samples, the pellets were crushed into granules and re-pelletized. For gas adsorption tests, 100% $H_2$ and CO were used, and sufficient amounts of gas were introduced to match the quantity of clusters present. After the sample was evacuated, 100% $H_2$ or 100% CO was introduced immediately using a gas valve. The XAFS data were analyzed using the xTunes software[39] for both X-ray absorption near-edge structure (XANES) and extended X-ray absorption fine structure (EXAFS). The $k^3$-weighted $\chi$ spectra (EXAFS spectra) in the $k$ ranges of 3.0–9.0 $Å^{-1}$ for the Pt $L_3$-edge and 3.0–18.0 $Å^{-1}$ for the Au $L_3$-edge were Fourier transformed into $r$ space (FT-EXAFS). The curve fitting analysis was conducted using FT-EXAFS spectra in the $r$ range of 1.8–3.2 Å for the Pt $L_3$-edge and 1.65–2.95 Å for the Au $L_3$-edge.

### Computational method

Density functional theory (DFT) calculations were conducted using the Gaussian 16 program.[40] The geometries and electronic energies of **PtAu8**, and CO-, $H_2$-, and H (hydride)-adsorbed **PtAu8** (abbreviated as CO-**PtAu8**, $H_2$-**PtAu8**, and H-**PtAu8**, respectively) were calculated using the B3LYP functional. LanL2DZ basis set was used for Au and Pt atoms and 6-31G* basis set was used for C, H, O, and P atoms. Frequency analyses were performed for **PtAu8**, CO-**PtAu8** and $H_2$-**PtAu8** to confirm that no imaginary frequencies were obtained at the optimized geometries. The optical properties of CO-**PtAu8** were also calculated by applying the time-dependent (TD) DFT method, solving 200 states, with the same functional and basis sets used in the ground state calculations. $H_2$/CO adsorption energies were obtained in the difference of Gibbs free energies between $H_2$/CO + **PtAu8** and $H_2$/CO-**PtAu8** where the electronic energies were replaced by calculations using B3LYP-D3 functional with the same basis sets to incorporate dispersion interactions.

Pt $L_3$-edge XANES calculations were performed with the Full Potential Multiple Scattering (FPMS) code[41] that employed the scattering potential without spherical potential approximation (Muffin-tin approximation). This code is based on Multiple-Scattering theory, which uses a multi-center expansion in spherical harmonics and a numerical solution of the local Schrödinger equation on each atomic site. In the overall calculation, $l_{max}$ is set at 8. H atoms bonded to the C atoms of the protecting ligands were not considered in the calculations because their contributions to the calculated XANES spectrum are negligible due to their long distance to the absorbing Pt atom (more than 4 Å) and their small scattering power. However, closer H atoms, as in the case of adsorption, were considered and demonstrated an effect on the spectra. Energy-dependent complex Hedin-Lundqvist potential[42,43] was used as the optical potential.

## Author contributions

S. Y. guided the whole experiment and conceived the idea. T. M. and S. K. drafted the manuscript. T. M. and

Published on 14 nuvembre 2024. Downloaded on 20/12/2025 2:52:36.

T. S. conducted the experiments, Y. O. developed analytical software for XAFS. U. S. carried out void analysis. S. K., J. O., and K. K. designed *in situ* cell for QXAFS. K. Hi., T. K. and T. U. designed the optical setup including measurement system for *in situ* QXAFS apparatus in SPring-8. K. N. gave some advice for structural analysis using low-temperature XAFS. K. Ha., Ka. Yo. and A. H. carried out XANES simulation. N. N. conducted energy calculation of clusters and gave some advice for DFT calculation results. K. S., Ke. Yo., K. Ya., and H. K. supported *in situ* XAFS measurements and discussed molecular diffusion. All the authors contributed to the final polishing of the manuscript.

## Data availability

The data supporting this manuscript is available in the ESI† and are available on request. Crystallographic data for **PtAu8-PMo12** has been deposited at the CCDC 2087794.

## Conflicts of interest

There are no conflicts to declare.

## Acknowledgements

This study was financially supported by NEDO (JPNP14004), JSPS KAKENHI (No. 22K14543, 24K01259, 24K17562, 24H02210, 24H02211, and 24H02217), Tokyo Metropolitan Government Advanced Research (R3-1), Tokyo Human Resources Fund for City Diplomacy, and Tokyo Metropolitan University Research Fund for Young Scientists. The synchrotron radiation experiment was performed in SPring-8 under the approval of the Japan Synchrotron Radiation Research Institute (JASRI) as 202407, 2023A1326, 2022B1259, 2021B1380.

## References

1 E. L. Albright, T. I. Levchenko, V. K. Kulkarni, A. I. Sullivan, J. F. DeJesus, S. Malola, S. Takano, M. Nambo, K. Stamplecoskie, H. Häkkinen, T. Tsukuda and C. M. Crudden, *J. Am. Chem. Soc.*, 2024, **146**, 5759–5780.
2 S. Li, N.-N. Li, X.-Y. Dong, S.-Q. Zang and T. C. W. Mak, *Chem. Rev.*, 2024, **124**, 7262–7378.
3 Y. Horita, M. Ishimi and Y. Negishi, *Sci. Technol. Adv. Mater.*, 2023, **24**, 2203832.
4 R. Jin, G. Li, S. Sharma, Y. Li and X. Du, *Chem. Rev.*, 2021, **121**, 567–648.
5 K. J. Taylor, C. L. Pettiette-Hall, O. Cheshnovsky and R. E. Smalley, *J. Chem. Phys.*, 1992, **96**, 3319–3329.
6 B. E. Salisbury, W. T. Wallace and R. L. Whetten, *Chem. Phys.*, 2000, **262**, 131–141.
7 R. H. Adnan, J. M. L. Madridejos, A. S. Alotabi, G. F. Metha and G. G. Andersson, *Adv. Sci.*, 2022, **9**, 2105692.
8 S. Hossain, D. Hirayama, A. Ikeda, M. Ishimi, S. Funaki, A. Samanta, T. Kawawaki and Y. Negishi, *Aggregate*, 2023, **4**, e255.
9 M.-M. Zhang, X.-Y. Dong, Y.-J. Wang, S.-Q. Zang and T. C. W. Mak, *Coord. Chem. Rev.*, 2022, **453**, 214315.
10 C. A. Smith, M. R. Narouz, P. A. Lummis, I. Singh, A. Nazemi, C.-H. Li and C. M. Crudden, *Chem. Rev.*, 2019, **119**, 4986–5056.
11 J. Olesiak-Banska, M. Waszkielewicz, P. Obstarczyk and M. Samoc, *Chem. Soc. Rev.*, 2019, **48**, 4087–4117.
12 Y. Shichibu and K. Konishi, *ChemNanoMat*, 2022, **8**, e202200194.
13 Z. Liu, L. Luo and R. Jin, *Adv. Mater.*, 2024, **36**, 2309073.
14 J. Foxley and K. L. Knappenberger Jr, *Annu. Rev. Phys. Chem.*, 2023, **74**, 53–72.
15 K. Kwak and D. Lee, *Acc. Chem. Res.*, 2019, **52**, 12–22.
16 L. Wang, J. Peng, Z. Tang, X. Kang, M. Fu and S. Chen, *Appl. Catal.*, 2018, **557**, 1–6.
17 Y. Zhu, H. Qian, M. Zhu and R. Jin, *Adv. Mater.*, 2010, **22**, 1915–1920.
18 X. Cai, G. Saranya, K. Shen, M. Chen, R. Si, W. Ding and Y. Zhu, *Angew. Chem., Int. Ed.*, 2019, **58**, 9964–9968.
19 K. Kwak, W. Choi, Q. Tang, M. Kim, Y. Lee, D.-E. Jiang and D. Lee, *Nat. Commun.*, 2017, **8**, 14723.
20 S. Takano, H. Hirai, T. Nakashima, T. Iwasa, T. Taketsugu and T. Tsukuda, *J. Am. Chem. Soc.*, 2021, **143**, 10560–10564.
21 H. Hirai, S. Takano, T. Nakashima, T. Iwasa, T. Taketsugu and T. Tsukuda, *Angew. Chem., Int. Ed.*, 2022, **61**, e202207290.
22 M. Schulz-Dobrick and M. Jansen, *Eur. J. Inorg. Chem.*, 2006, 2006, 4498–4502.
23 M. A. Aubart and L. H. Pignolet, *J. Am. Chem. Soc.*, 1992, **114**, 7901–7903.
24 R. P. F. Kanters, P. P. J. Schlebos, J. J. Bour, W. P. Bosman, H. J. Behm and J. J. Steggerda, *Inorg. Chem.*, 1988, **27**, 4034–4037.
25 D. A. Krogstad, W. V. Konze and L. H. Pignolet, *Inorg. Chem.*, 1996, **35**, 6763–6771.
26 L. N. Ito, J. D. Sweet, A. M. Mueting, L. H. Pignolet, M. F. J. Schoondergang and J. J. Steggerda, *Inorg. Chem.*, 1989, **28**, 3696–3701.
27 T. Matsuyama, S. Kikkawa, Y. Fujiki, M. Tsukada, H. Takaya, N. Yasuda, K. Nitta, N. Nakatani, Y. Negishi and S. Yamazoe, *J. Chem. Phys.*, 2021, **155**, 044307–044314.
28 Y. Fujiki, T. Matsuyama, S. Kikkawa, J. Hirayama, H. Takaya, N. Nakatani, N. Yasuda, K. Nitta, Y. Negishi and S. Yamazoe, *Commun. Chem.*, 2023, **6**, 129.
29 C. F. Macrae, I. Sovago, S. J. Cottrell, P. T. A. Galek, P. McCabe, E. Pidcock, M. Platings, G. P. Shields, J. S. Stevens, M. Towler and P. A. Wood, *J. Appl. Crystallogr.*, 2020, **53**, 226–235.
30 S. N. Reifsnyder, M. M. Otten, D. E. Sayers and H. H. Lamb, *J. Phys. Chem. B*, 1997, **101**, 4972–4977.
31 J. J. Bour, R. P. F. Kanters, P. P. J. Schlebos, W. P. Bosman, H. Behm, P. T. Beurskens and J. J. Steggerda, *Recl. Trav. Chim. Pays-Bas*, 1987, **106**, 157–158.

 This journal is © The Royal Society of Chemistry 2025

Published on 14 nuvembre 2024. Downloaded on 20/12/2025 2:52:36.

32 P. Glatzel, J. Singh, K. O. Kvashnina and J. A. van Bokhoven, *J. Am. Chem. Soc.*, 2010, **132**, 2555–2557.
33 N. Mehio, S. Dai and D.-E. Jiang, *J. Phys. Chem. A*, 2014, **118**, 1150–1154.
34 S. Seino, R. Kawahara, Y. Ogasawara, N. Mizuno and S. Uchida, *Angew. Chem., Int. Ed.*, 2016, **55**, 3987–3991.
35 S. M. Perera, S. R. Hettiarachchi and J. W. Hewage, *ACS Omega*, 2022, **7**, 2316–2330.
36 J. J. Bour, P. P. J. Schlebos, R. P. F. Kanters, M. F. J. Schoondergang, H. Addens, A. Overweg and J. J. Steggerda, *Inorg. Chim. Acta*, 1991, **181**, 195–200.
37 T. Matsuyama, J. Hirayama, Y. Fujiki, S. Kikkawa, W. Kurashige, H. Asakura, N. Kawamura, Y. Negishi, N. Nakatani, K. Hatada, F. Ota and S. Yamazoe, *J. Phys. Chem. C*, 2021, **125**, 3143–3149.
38 T. Uruga, M. Tada, O. Sekizawa, Y. Takagi, T. Yokoyama and Y. Iwasawa, *Chem. Rec.*, 2019, **19**, 1444–1456.
39 H. Asakura, S. Yamazoe, T. Misumi, A. Fujita, T. Tsukuda and T. Tanaka, *Radiat. Phys. Chem.*, 2020, **175**, 108270–108273.
40 M. J. Frisch, G. W. Trucks, H. B. Schlegel, G. E. Scuseria, M. A. Robb, J. R. Cheeseman, G. Scalmani, V. Barone, G. A. Petersson, H. Nakatsuji, X. Li, M. Caricato, A. V. Marenich, J. Bloino, B. G. Janesko, R. Gomperts, B. Mennucci, H. P. Hratchian, J. V. Ortiz, A. F. Izmaylov, J. L. Sonnenberg, D. Williams-Young, F. Ding, F. Lipparini, F. Egidi, J. Goings, B. Peng, A. Petrone, T. Henderson, D. Ranasinghe, V. G. Zakrzewski, J. Gao, N. Rega, G. Zheng, W. Liang, M. Hada, M. Ehara, K. Toyota, R. Fukuda, J. Hasegawa, M. Ishida, T. Nakajima, Y. Honda, O. Kitao, H. Nakai, T. Vreven, K. Throssell, J. A. Montgomery Jr., J. E. Peralta, F. Ogliaro, M. J. Bearpark, J. J. Heyd, E. N. Brothers, K. N. Kudin, V. N. Staroverov, T. A. Keith, R. Kobayashi, J. Normand, K. Raghavachari, A. P. Rendell, J. C. Burant, S. S. Iyengar, J. Tomasi, M. Cossi, J. M. Millam, M. Klene, C. Adamo, R. Cammi, J. W. Ochterski, R. L. Martin, K. Morokuma, O. Farkas, J. B. Foresman and D. J. Fox, *Gaussian 16, Revision B.01*, Gaussian, Inc., Wallingford CT, 2016.
41 K. Hatada, K. Hayakawa, M. Benfatto and C. R. Natoli, *J. Phys.: Condens. Matter*, 2010, **22**, 185501.
42 L. Hedin and S. Lundqvist, *Solid State Phys.*, 1970, **23**, 1–181.
43 L. Hedin and B. I. Lundqvist, *J. Phys. C: Solid State Phys.*, 1971, **4**, 2064.